Publications of the Astronomical Society of Australia (PASA), Vol. 30, e037, 15 pages.

doi:10.1017/pasa.2013.15

The Multiple Star η Muscae

E. Budding[1,2,3,6], R. Butland[4] and M. Blackford[5]

[1]School of Chemical and Physical Sciences, Victoria University of Wellington, Wellington, New Zealand
[2]Department of Physics and Astronomy, University of Canterbury, Christchurch, New Zealand
[3]Carter Observatory, Wellington, New Zealand
[4]Royal Astronomical Society of New Zealand, Wellington, New Zealand
[5]Variable Stars South, Wellington, New Zealand
[6]E-mail: ed.budding@gmail.com

(Received April 3, 2013; Accepted May 17, 2013; Online Publication June 20, 2013)

Abstract

High-resolution spectroscopy of η Mus is combined with literature and new photometry to provide a comprehensive analysis of its components. Our main absolute parameters for the close binary system are M_1 and M_2 3.34 ± 0.04 $M_\odot$, R_1 2.13 ± 0.07 $R_\odot$, R_2 2.34 ± 0.10 $R_\odot$; T_1 $13\,000 \pm 300$, T_2 $12\,600 \pm 300$, K; and distance 125 ± 10 pc. Our findings update earlier results in a number of respects. We thus confirm that η Mus B is a gravitationally bound companion of the close binary. This relates to the variable γ velocity of the radial velocities of η Mus A. We connect this to the recently discovered member η Mus D, whose orbit we link to new data. We also provide a spectroscopic examination of the Ap star η Mus B, listing over 450 identified lines. We argue that the system is still young, and the apparently anomalous rotation of the close binary's secondary can be reconciled with its being a physically larger star, still condensing to the zero-age main sequence. Models of young condensing stars permit such expanded states, particularly during the deuterium-burning stage, and our results are in agreement with appropriate low-age models. This possible configuration may make η Mus an important example for testing young star models, formation, and evolution scenarios. This multiple star can be compared with V831 Cen and the general properties related to its membership of the Sco–Cen OB2 association.

Keywords: binaries: close – binaries: eclipsing – stars: evolution – stars: fundamental parameters – open clusters and associations – stars: individual: η Mus

1 INTRODUCTION

The multiple star η Mus (HD 114911, HIP 64661, and HR 4993) contains a bright ($V \sim 4.8$–4.9, $B - V \approx -0.08$, $U - B \approx -0.34$, $V - J \approx -0.18$, $J - K \approx -0.04$) young B8V-type eclipsing binary, located on the sky at about 58 arcsec from a 7.3-mag visual companion η Mus B (CD $-$ 67 1384B) and within $\sim$3 arcsec of a 10th-mag (J) closer companion (η Mus C = DUN 131C). The chemical peculiarity of η Mus B was reported by Bidelman & McConnell (1973) and checked using a Stromgren photometric technique by Vogt & Faúndez (1979). Renson & Manfroid (2009) assign the spectral classification (A1 Sr, Cr, and Eu) to this star. Butland & Budding (2011) announced the likely presence of an additional relatively close (period $\sim$5 yr) component we refer to as η Mus D.

As with V831 Cen (Budding, İnlek, & Demircan 2010), the sky location, *Hipparcos* distance 124 ± 9 pc, and proper motions ($\mu_\alpha \cos\delta = -36.92$, $\mu_\delta = -10.63$ mas yr^{-1}) indicate the system to be a likely member of the Lower Centaurus Crux (LCC) concentration (Blaauw 1964; de Zeeuw, Hoogerwerf, & de Bruijne 1999) of the Sco–Cen OB2 association, within the Gould's Belt giant star formation region (Nitschelm 2004). This setting makes the system of special interest for star formation studies and understanding the nature of gravitationally bound systems within young star associations. That close binaries can reveal stellar absolute parameters with relatively high precision adds further motivation (Budding 2008). General background has been given by R. Idaczyk et al. (in preparation).

Eclipses were discovered as a consequence of *Hipparcos* photometry (ESA 1997), from which a period of about 2.4 d was found. The classical 'EA' type light curve suggests two relatively well-separated stars, although the shallow minima might be associated with a third light.

The Tokovinin (1997) catalogue of multiple stars includes an estimate of the period of the wide system at around 200 000 yr, and masses of the close (eclipsing) components as 4.48 and 2.63 $M_\odot$, with η Mus B at 3.20 $M_\odot$. Hubrig et al. (2001) re-evaluated the mass ratio as $M_1/M_2 = 1.14$ (cf. Tokovinin's value of 1.70, although recent values are still closer to unity). Hubrig et al. (2001), whilst examining the star for a

possible X-ray source using ESO's adaptive optics system ADONIS with the 3.6-m telescope on La Silla, discovered the additional companion η Mus C, which they identified as a pre-main-sequence (PMS) object, separated by 2.71 arcsec at position angle 125°, having magnitude differences 5.25, 4.54, and 3.32 in the J, H, and K bands.

The present article continues the southern binaries programme started at the Astrophysics Research Centre, 18th March University of Çanakkale and the Carter Observatory, New Zealand, utilising eclipsing binary system analysis (for further background, see Budding et al. 2009, 2010; hereafter Papers I and II). The arrangement of this paper follows along similar lines. A previous related study was that of Bakış et al. (2007), whose radial velocity (RV) amplitudes we are in good agreement with. There are differences in analysis methods between Bakış et al. and the present contribution, however, and also our inferences are significantly different, particularly after the identification of η Mus D, as well as our 'occultation' assessment of the primary eclipse.

In the following section, we discuss photometry of η Mus, including our own new data. Section 3 presents spectroscopic material, with observational background and details on data reduction and analysis including rotation and RV derivations. From these results, in Section 4 we determine absolute parameters of the stars in the close binary system. Section 5 gives information about the other three known components of this multiple star and the final discussion (Section 6) attempts to provide a coherent account of η Mus, in particular addressing the issues of the secondary's greater size and gravitational binding of the wide (AB) binary.

2 PHOTOMETRIC ANALYSIS

We have approached photometric analysis for close binaries such as η Mus using a few general inferences on key parameters. The $B - V$ and $U - B$ colours given above agree with the B8V type reported in the SIMBAD database. Similarly, Slawson's (1992) colours, when dereddened ($(B - V)_0 = -0.10$, $(U - B)_0 = -0.37$), are suggestive of a spectral type around B7.5. A primary temperature of ∼12 000 K can be posited (Budding & Demircan 2007), although Sokolov (1995) gave a much higher representative temperature for the pair as 16 130 ± 960 K, from analysis of the ultraviolet continuum slope. On the other hand, Hubrig et al. (2001) estimated the mean effective temperature at 12 760 K, from Geneva system colours, while Flower's (1996) calibration yields a temperature about 1000 K less than this.

Later, we give reasons for preferring effective temperatures that are closer to the Hubrig et al. estimate, although we can note that light-curve fittings show the geometrical elements to be not so sensitive to changes of the effective temperatures within several percent of their set values. Still, the primary should be a few hundred K hotter than the secondary to account for the observed differences in eclipse depths.

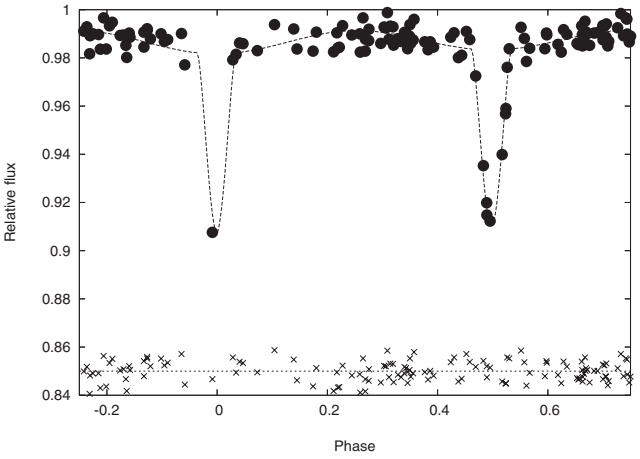

Figure 1. *Hipparcos V* photometry of η Mus and model fitting. The residuals, shifted by 0.85 on the flux axis, are shown below the curve fit.

Table 1. Initial curve-fitting results for the *Hipparcos* photometry of η Mus

Parameter	Value	Error
Primary effective temperature T_h (K)	12 000	
Secondary effective temperature T_c (K)	11 200	
Mass ratio M_2/M_1	1.0	
Primary fractional luminosity L_1	0.59	0.06
Secondary fractional luminosity L_2	0.41	0.06
Primary relative radius r_1 (mean)	0.168	0.007
Secondary relative radius r_2 (mean)	0.146	0.008
Orbital inclination i (deg)	76.9	0.5
Primary limb darkening u_1	0.35	
Secondary limb darkening u_2	0.37	
Corr. to phases $\Delta\phi_0$ (deg)	0.82	0.3
Goodness of fit χ^2/ν	1.11	
Data-point accuracy Δl	0.004	

2.1 *Hipparcos* data

We first examined the *Hipparcos* (V) light curve (Figure 1), which points to a relatively low inclination or perhaps a third light. Our main tool for photometric analysis involves the Information Limit Optimisation Technique (ILOT) presented by Banks & Budding (1990). More background on this, including its physically realistic fitting function, was given by Budding & Demircan (2007, chapter 9).

The curve fit shown corresponds to the parameter set listed, with formal errors, in Table 1. Symbols have their conventional meanings and further details are given in the references of the preceding paragraph. This optimal fitting shows that an acceptable result can be found with inclination ∼76°, but without significant third light, although the primary minimum is very poorly covered. Using the known colours and spectral types, a trial MS-like model can be made from two similar stars with total mass close to 7 $M_\odot$. The period of 2.3963 d, together with Kepler's third law and the provisionally adopted masses, yields a separation of about 14.4 $R_\odot$. A corresponding typical MS pair would have undistorted mean

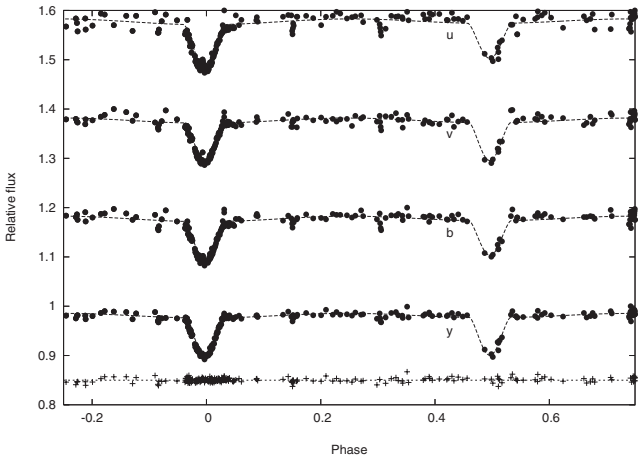

Figure 2. Light-curve fittings applied to the *uvby* photometry of η Mus, as presented by Hensberge et al. (2007). The relative fluxes are shown against phase with each curve vertically displaced by a linear displacement of 0.2. A greater primary depth in *u* is apparent, although the relative depths of the two minima are not so different at other wavelengths. No indication of a third light was found in this analysis. The residuals for the *y* fitting, shifted to 0.85, are shown at the bottom.

radii of about 2.4 $R_\odot$, implying relative radii r of around 0.17, not far from those found from the *Hipparcos* data analysis in Table 1. We adopt a mass ratio of unity in Table 1, anticipating the spectroscopic results discussed below, although the geometric parameters pertaining to the eclipse shapes are not significantly perturbed with the Hubrig et al. (2001) mass ratio. The lower secondary radius r_2 given in Table 1 does not directly reconcile with close similarity of the two stars, expected from the similarity of the two eclipse depths. The primary minimum is so poorly covered in the *Hipparcos* photometry, however, that it would be unwise to put weight on this initial fitting: it should be regarded rather as a guide.

2.2 Light curves of Hensberge et al.

Starting from such preliminaries, ILOT type analysis was applied to the more extensive *uvby* photometry, kindly supplied by Dr H. Hensberge (Hensberge et al. 2007; Figure 2). The essentially unity value of the spectroscopic mass ratio found below was used. There was fair agreement on the geometric parameters when determined separately (i.e. they were all within their probable errors), also with the *Hipparcos* light curve. We also found a small shift to the zero point of the phases (0.0040) calculated from the ephemeris of Hensberge et al. (2007). Bakış et al. (2007) noted, from the high dispersion spectroscopy, a greater apparent rotation speed of the secondary than the primary (see also Section 3.1).

We then considered the possibility that the secondary is larger than the primary, and an occultation model for the primary eclipse proved to yield similar or slightly lower χ^2 values to the fittings. Table 2 lists our finally adopted geometric parameters corresponding to an optimal modelling of the photometric data. An appreciable scale to the errors

Table 2. Summary results of fitting the light-curve data on η Mus from Hensberge et al. (2007) for the main geometric parameters

Parameter	Value	Error
T_h (K)	12 500	
T_c (K)	12 200	
M_2/M_1	1.0	
r_1 (mean)	0.150	0.005
r_2 (mean)	0.165	0.008
i (deg)	76.4	0.4
χ^2/ν	1.00	
Δl	0.005	

Table 3. Colour-dependent parameters in the η Mus close binary: luminosities of primary m_1 and secondary m_2 (in mag); linear limb-darkening u_1, u_2; gravity brightening τ_1, τ_2 and reflection effect coefficients E_1, E_2

	R	*V*	*y*	*b*	*B*	*v*	*u*
m_1	5.72	5.68	5.67	5.57	5.60	5.68	6.34
m_2	5.47	5.39	5.40	5.41	5.37	5.51	6.26
u_1	0.27	0.33	0.33	0.38	0.39	0.40	0.41
u_2	0.28	0.34	0.34	0.39	0.40	0.41	0.42
τ_1	0.54	0.59	0.60	0.67	0.70	0.75	0.86
τ_2	0.55	0.61	0.62	0.69	0.70	0.75	0.86
E_1	0.50	0.56	0.56	0.65	0.68	0.74	0.85
E_2	0.59	0.66	0.67	0.71	0.73	0.78	0.88

The errors of these empirically determined component magnitudes m_1 and m_2 are estimated to be 0.02 mag. The other parameters are adopted from the theoretical work of van Hamme (1993) (*u*), von Zeipel (1924) (τ), and Hosokawa (1958) (*E*).

results from calculating them with proper account of parameter interdependence.[1] This reflects an inherent relatively low determinacy of curve fittings associated with these fairly shallow eclipses. Table 3 lists the magnitudes of either eclipsing star using the *ubvy* magnitudes of the main comparison (HD 114570) given by Hensberge et al. The secondary star is the more luminous in our model, but it can be seen that the primary becomes relatively brighter at shorter wavelengths, in keeping with a somewhat higher temperature. We discuss this point further in Sections 4 and 6. The relatively small proximity effects are evaluated as described in the CURVEFIT manual of Rhodes (2008) corresponding to the assigned effective temperatures and *uvby* filter wavelengths.

Hensberge et al. (2007) also referred to photometry during the interval 1983–1990, their analysis of which resulted in a refined period of 2.396320 d. We will discuss this in Section 5.

2.3 DSLR photometry

We have obtained more recent times of minima of η Mus using the developing technology of digital single lens reflex

[1] Section 9.4 of Budding & Demircan (2007) gives more background on this issue and the determination of formal errors.

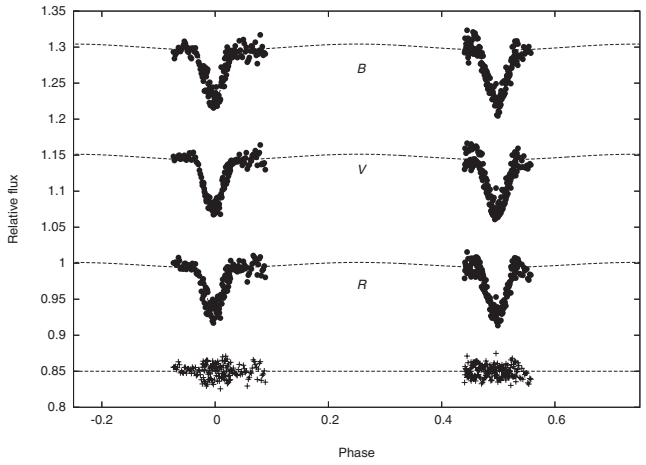

Figure 3. Light-curve fittings applied to our *BVR* photometry of η Mus (see also Section 5.3). The *R* residuals are shown below, where the straight line at 0.85 guides the eye.

(DSLR) camera photometry (Blackford & Schrader 2011). These developments come under the southern binaries monitoring program of the Variable Stars South (VSS) section of the Royal Astronomical Society of New Zealand (RASNZ). The data were gathered using an unmodified Canon 450D (Digital Rebel XSi) and Nikkor 180-mm lens operated at f4. Instrumental magnitudes obtained from differential aperture photometry, using four comparison stars, were corrected for atmospheric extinction and transformed to the standard system. We have stacked five minima observed in this way in Figure 3, where we also show optimal fits to the reduced *B*, *V*, and *R* data sets. One of the comparison stars was not in the frame for the first eclipse, and while this appeared to introduce a small shift of the out-of-eclipse reference flux, it does not disturb the shape or time of minimum. Keeping in mind the large number of individual measurements, the quality of the fits, as judged by the resulting reduced χ^2 values, is quite comparable to those for the *uvby* data, and the corresponding geometrical parameters are essentially the same as those of Table 2, allowing confidence in the assigned error estimates.

3 SPECTROSCOPY

Our spectroscopic data were taken with the High Efficiency and Resolution Canterbury University Large Échelle Spectrograph (HERCULES) of the Department of Physics and Astronomy, University of Canterbury (cf. Hearnshaw et al. 2002). This was used with the 1-m McLellan telescope at the Mt John University Observatory (MJUO; ~43°59′S, 174°27′E). Further information is given in Paper I (see also Skuljan, Ramm, & Hearnshaw 2004; Bakış et al. 2007; R. Idaczyk et al. in preparation). A 100-μm (slitless) optical fibre was used, enabling a resolution of approximately 41 000. A microlens in front of the fibre speeds up the focal ratio to an effective *f*/4.5 optical system, so that its 100-μm entrance pupil corresponds to about 4.3 arcsec on the sky. This accommodates the moderate-to-poor seeing conditions generally obtained. Average exposure times were about 200 s, which yield a signal-to-noise ratio (S/N) of ~100 in the selected spectral region (between ~470 and ~670 nm).

Some 50 separate exposures on η Mus were made on seven nights in the (southern) autumn of 2006, and most of these (43) were in the short interval May 17–20. These observations were made with a Spectral Instruments SITe series (1024 × 1024 pixels) camera. The camera only covers part of the whole spectral range, arranged to provide a region of good sensitivity. A further seven spectra were taken on August 19–20 and September 9 after the SITe camera had been replaced by an SI600s type. This camera has a larger number of smaller pixels (by a factor of ~0.60) to cover the whole field effectively in a 4096 × 4096 array. Two exposures of the visual companion (η Mus B) were included in this later period. Measurements based on these data from 2006 were first presented by Bakış et al. (2007). Several more exposures of both η Mus A and B have been taken since 2010. We have independently examined all these data for the present paper. Although many of our results are very similar to those of Bakış et al. (2007), there are some significant differences that will appear in what follows.

Initial data acquisition and reduction was performed with the on-site software package HRSP (Skuljan & Wright 2007); however, the change of camera during the program entailed the use of different versions of HRSP. Version 4, used for much of the reductions presented here, allows results from the two camera formats to be easily compared, as well as being portable and robust.[2]

The two-dimensional wavelength calibration in HRSP uses several hundred of the available Th/Ar reference lines (Skuljan et al. 2004). The static, highly controlled arrangement of HERCULES means that this calibration changes little from exposure to exposure (shifts up to tens of m s^{-1}). Some further details about the performance of this spectrograph are given by R. Idaczyk et al. (in preparation).

HRSP stores processed data as 'FITS' files, which is convenient for further analysis using IRAF (cf. Barnes 1993),[3] or other programs such as our SPECTRUM module that we used in deriving RV values (see Section 3.2). Identifiable spectral lines for this close binary are given in Table 4, together with their central relative depths. The lines are similar to those listed for U Oph in Paper I, although corresponding to a slightly cooler spectral type. Unlike Paper II, where the relative effects of proximity and noise were large for V831 Cen, they are reduced in the case of η Mus. The two He I lines (6678 and 5875) were well placed for RV determinations, as also the Fe II line at 5169. Two of the lines used by Bakış et al. (2007) were found unsuitable for precise measurement.

[2] It will run via Cygwin on an MS Windows platform.

[3] IRAF is distributed by the National Optical Astronomy Observatories, operated by the Association of Universities for Research in Astronomy Inc. (AURA) under cooperative agreement with the National Science Foundation.

Table 4. Lines in the spectra (camera subfield 2) of η Mus used for RV determinations

Species	Order no.	Reference wavelength	Relative depth	Comment
He I	85	6678.149	0.030	ms
Si II	89	6371.359	0.029	ms
He I	97	5875.65	0.056	sd
Fe II	107	5316.693	0.020	dmw
Fe II	110	5169.030	0.030	ms
Fe I	113	5041.074	0.023	wd
He I	121	4713.258	0.021	dmw
Fe II	124	4583.829	0.020	w
Fe II	125	4549.467	0.022	w

The comments correspond to—ms: moderately strong; sd: strong but sometimes distorted; dmw: doublet moderately weak; wd: weak sometimes distorted; w: weak.

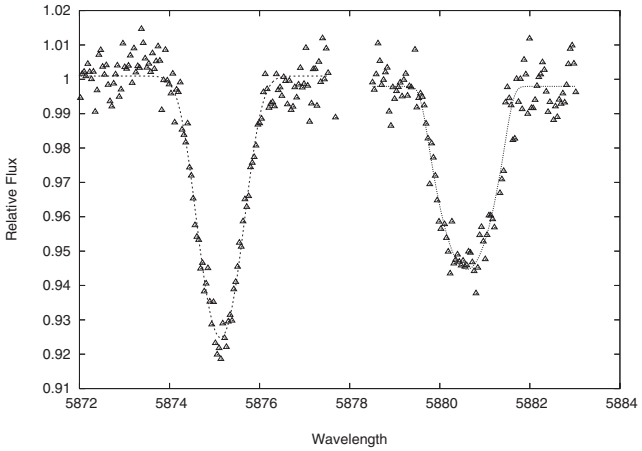

Figure 4. Results of profile fitting to the He I 5875 lines at elongation. The secondary is on the right.

The Mg I 5173 line was seldom visible and the Fe II 5018 line was often blended and distorted.

3.1 Rotational velocities

We fitted selected helium line profiles of η Mus at elongation phases using our computer program PROF2. Results are shown in Figure 4 with parameters listed in Table 5.

Meanings of the parameters in Table 5 were explained in Paper I. For this particular pair of lines (from spectrum 34 in Table 6), the parameter r, measuring the mean projected rotational velocity, yields values of 42 ± 1 and 54 ± 2 km s^{-1} for primary and secondary components, respectively, after division by sin i. These values may be compared with those derived from corotation with the systemic rotation of 300 km s^{-1} and the fractional radii from Table 2. This would produce equatorial speeds of 45 ± 2 and 49 ± 3 km s^{-1}, respectively, in the occultation primary photometric model of the system.

Although it is clear, both from these results and those of Bakış et al. (2007), that the secondary rotates faster than the primary, this result is still not highly precise. The use

Table 5. Profile fitting parameters for absorption lines

η Mus A, He I 5875		
Parameter	Value	Error
Primary		
I_c	1.0009	0.0004
I_d	0.0732	0.0014
λ_m	5875.132	0.007
r	0.804	0.010
s	0.32	0.015
χ^2/ν, Δl	1.03	0.005
Secondary		
I_c	0.9979	0.0005
I_d	0.0457	0.0021
λ_m	5880.601	0.009
r	1.026	0.025
s	0.10	0.10
χ^2/ν, Δl	1.21	0.005

of the IRAF SPLOT profile fitter on 65 line pairs produced a secondary/primary mean line width ratio of 1.31 ± 0.23, the error measure being associated with the appreciable scatter for many of the lines, whose maximum depths are still only a few percent of the continuum. The above fitting, for a relatively well-defined pair, confirms this result (ratio $= 1.28 \pm 0.10$), although somewhat at variance with our photometric ratio (1.08 ± 0.08). The measured rotation speeds are, however, within their standard deviations of corotation. Asynchronous rotation of one or other star is still not outside the bounds of possibility, nor is the transit primary option for the photometric analysis. However, the secondary's relatively high rotation is firmly evidenced, both by Bakış et al. (2007) and ourselves. We must therefore give reasonable consideration to the possibility of a corotating, but enlarged, secondary star. Stars in an arrangement such as η Mus should normally synchronise within ~1 Myr (Vaz, Andersen, & Claret 2007). We discuss this point further in Section 6.

3.2 Radial velocities

The RV measurements involved only strong lines, as listed in Table 4. If more than one line was present in an order, only the most clearly defined one was used. Our Python module SPECTRUM, written to speed up the process of RV determination from line shifts, uses the open source SciPy library's OPTIMIZE subpackage and its least-squares module CURVE_FIT to fit a rotation-broadened profile to the selected spectral lines. Typically ~10 lines spread across the available spectral range were initially selected. Manual identification of useful lines is first carried out with the aid of IRAF's SPLOT command. High S/N lines with good visibility that lack significant telluric contamination are favoured. It can be deduced from Figure 4 that for orbital phases within about ±0.03 of 0.0 or 0.5 lines from the components will overlap to some extent. Three or four exposures among the 43 listed in Table 6 are

Table 6. Radial velocity data for η Mus (2006 May)

No.	HJD −2450000 d	Phase	RV1 ± km s^{-1}		RV2 ± km s^{-1}		γ km s^{-1}
1	3872.8828	0.421	− 44.8	2.2	92.9	1.9	24.0
2	3872.9803	0.461	− 10.0	1.9	60.3	3.7	25.1
3	3872.9869	0.464	− 8.4	2.9	56.7	3.5	24.1
4	3873.0727	0.500	25.6	0.4	19.8	2.2	22.7
5	3873.1447	0.530	53.8	0.9	− 1.9	4.0	25.9
6	3873.1486	0.532	55.5	1.5	− 8.1	2.5	23.7
7	3873.8006	0.804	160.3	2.1	− 116.4	2.9	21.9
8	3873.8046	0.805	160.0	2.4	− 115.4	3.1	22.3
9	3873.8250	0.814	156.4	2.6	− 111.4	3.2	22.5
10	3873.8292	0.816	155.4	2.8	− 110.3	3.5	22.5
11	3873.8613	0.829	151.0	3.0	− 106.2	3.1	22.4
12	3873.8651	0.831	149.8	2.3	− 104.9	2.9	22.5
13	3873.9276	0.857	137.1	1.8	− 91.2	1.9	23.0
14	3873.9325	0.859	134.4	1.5	− 89.5	2.1	22.4
15	3874.0311	0.900	109.3	2.6	− 62.9	2.0	23.2
16	3874.0371	0.902	108.0	3.3	− 62.1	3.6	22.9
17	3874.0719	0.917	96.1	1.9	− 49.4	2.1	23.3
18	3874.0748	0.918	95.2	2.5	− 47.9	2.0	23.6
19	3874.1274	0.940	77.2	2.8	− 28.5	3.3	24.3
20	3874.1320	0.942	75.9	2.9	− 24.5	3.8	25.7
21	3874.1900	0.966	52.8	2.6	− 6.6	4.0	23.1
22	3874.1940	0.968	48.6	4.3	− 10.6	6.7	19.0
23	3874.2447	0.989	27.8	5.5	8.0	8.6	17.9
24	3874.2491	0.991	23.0	8.3	20.4	3.2	21.7
25	3874.7880	0.216	− 116.8	3.2	163.6	4.1	23.4
26	3874.7921	0.218	− 119.0	2.6	167.1	2.8	24.1
27	3874.8384	0.237	− 120.9	2.8	168.1	3.1	23.6
28	3874.8426	0.239	− 122.9	2.8	167.2	3.1	22.2
29	3874.8943	0.260	− 122.2	2.0	169.6	3.2	23.7
30	3874.8991	0.262	− 120.2	3.2	167.8	3.1	23.8
31	3874.9317	0.276	− 121.1	2.9	166.4	3.0	22.6
32	3874.9356	0.277	− 118.5	3.0	165.5	4.4	23.5
33	3874.9797	0.296	− 113.3	2.9	163.4	2.7	25.0
34	3874.9837	0.297	− 114.1	2.4	162.3	3.3	24.1
35	3875.0247	0.315	− 108.4	2.3	156.9	2.9	24.3
36	3875.0799	0.338	− 100.4	2.5	145.6	3.5	22.6
37	3875.0856	0.340	− 98.6	2.2	145.5	2.6	23.5
38	3875.1290	0.358	− 87.8	2.8	134.5	3.2	23.4
39	3875.1897	0.383	− 73.2	2.6	122.8	2.7	24.8
40	3875.1951	0.386	− 72.7	3.1	121.0	3.2	24.1
41	3876.0147	0.728	167.0	4.4	− 121.7	3.0	22.6
42	3876.0708	0.751	168.3	2.5	− 122.4	2.1	23.0
43	3876.0954	0.761	167.9	2.9	− 122.4	2.2	22.7

thus affected. Although all the listed observations are shown in Figure 6, the inclusion of these near-conjunction points in the fitting does not alter the resultant parameter specifications by more than their probable errors. Reference wavelengths of the selected lines were taken from the ILLSS website.[4] As SPECTRUM runs, selected images are displayed together with a profile fitting. Barycentric velocities are calculated, examined, stored, and averaged over (usually nine) lines.

The 2006 May schedule of timings, heliocentric corrected RV (RV1, and RV2) and systemic RV (γ) measures are given in Table 6. The errors of mean line centre positions in Table 6, typically $\sim$2.0 km s^{-1}, are estimated, from internal agreements of the separate measures.

The longer wavelength lines can be affected by telluric intrusions that can vary in strength from exposure to exposure. Visual inspection is then useful, taking into account S/Ns, and RV measures derived from SPECTRUM were checked against eye-based measurements.

The RVs were also checked by inter-correlating selected spectral regions. A result is shown in Figure 5. It is of interest to compare this diagram with results obtained from the procedures mentioned above. It seems clear that spectral irregularities or window positioning affect any cross-correlation function (ccf) symmetry that might apply to an idealised case. These irregularities extend to the peak and influence its location at the level of several km s^{-1}. Such effects can be noticed in Figure 1 of Bakış et al. (2007) (see also Rucinski 2002).

[4] http://vizier.u-strasbg.fr/cgi-bin/VizieR?-source=V1/71A/illss

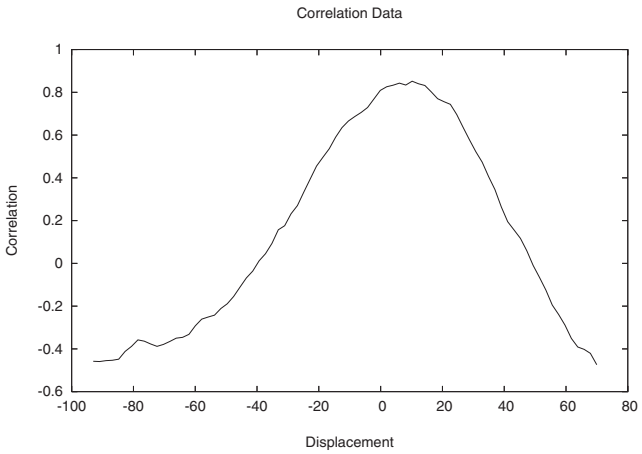

Figure 5. Cross-correlation of the two He I 6678 lines corresponding to image 38 in Table 6. The abscissae are in km s^{-1}, while ordinates are normalised to unity at perfect correspondence and scaled so that the average deflection in a window is zero. This will entail some anti-correlation as the two line absorption peaks move apart. The two equal window locations have a velocity separation of 206.2 km s^{-1}, so the net displacement of the two lines indicated by the ccf peak shift of 10.2 km s^{-1} is 216.4 km s^{-1}, which may be compared with 222.3 km s^{-1} from the measures in Table 6. The ccf reflects line asymmetries, particularly of the secondary, whose lines tend to show less slope on the primary-facing side. High-frequency noise also affects the peak region. It is true that readjustment of the correlation windowing after a preliminary result as shown here can result in a closer agreement with the RVs of Table 6; however, the diagram shows that cross-correlation procedures to derive good RVs are not necessarily straightforward (cf. Rucinski 2002).

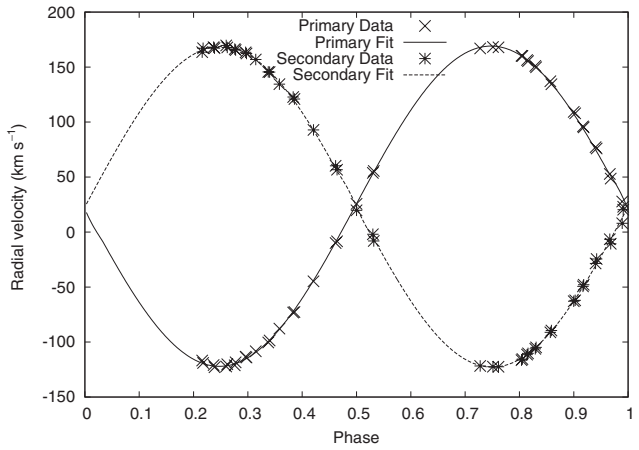

Figure 6. Measured RVs are plotted against a fitting function that takes into account both proximity and eclipse effects. The primary (higher T_e) star approaches (more negative RVs relative to the centre of mass) after phase zero. The inclination is sufficiently low as to render the Rossiter–McLaughlin effect insensible.

We used the same model for fitting the RV variations (FITRV4A) as in Papers I and II. Proximity effects such as reflection and non-spherical stellar distortions are not significant for the present case, although the fitting program automatically includes them. Results are shown in Figure 6 and corresponding parameters given in Table 7. Although the close binary must have some level of dynamical interaction with its companion stars, perturbations to the close orbit are small, and, keeping in mind the findings of Zahn (1977), *a priori* neglect of any eccentricity in the analysis is reasonable.

Table 7. Adopted absolute parameters for the η Mus A close binary. Formal errors are shown in parentheses to the right and relate to the least significant digits in the corresponding parameter values

Parameter	Value
Period (days)	2.396318
Epoch (HJD)	2453874.2708
Magnitudes V, $(B-V)$, $(V-J)$	4.774; −0.077; −0.175
Velocity amplitudes $K_{1,2}$ (km s^{-1})	145.6 (3); 145.8 (4)
Star separation A ($R_\odot$)	14.19 (5)
System velocity V_γ (km s^{-1})	23.2 (3)
Masses $M_{1,2}$ ($M_\odot$)	3.34(4); 3.34 (4)
Radii $R_{1,2}$ ($R_\odot$)	2.13(7); 2.34 (10)
Surface gravity g (log cgs)	4.30; 4.22
Primary magnitude V_1	5.68 (2)
Secondary magnitude V_2	5.40 (2)
Primary temperature $T_{e,1}$ (K)	13 000 (300)
Secondary temperature $T_{e,2}$ (K)	12 600 (300)
Distance	125 (10) pc

4 ABSOLUTE PARAMETERS

The RV solutions shown in Figure 6 correspond to the $K_{1,2}$ amplitudes given in Table 7. The two amplitudes are essentially equal to within their measurement accuracy, although the two spectra are distinctly different as seen in Figure 4. The orbital semimajor axis is derived given the adopted inclination (76.°5). Kepler's law then allows the shown masses to be obtained. The radii come from multiplying the orbit's radius by the fractional radii given in Table 2. The velocity of the centre of mass V_γ corresponds to the adopted epoch for those few days in 2006 May (JD2453874.2708) whose data were used for the RV curve fittings. The masses and radii of Table 7 are in reasonable agreement with the B8V spectral types and corresponding effective temperatures given in Section 1, according to Table 3.6 in Budding & Demircan (2007), while the slightly shallower secondary minima (at shorter wavelengths) go with its temperature decrement. This is in agreement with the luminosity and radius ratios derived from Table 7.

With the *Hipparcos* parallax, the absolute V magnitudes are 0.21 and −0.08 for the primary and secondary, respectively. According to their masses and recent Padova modelling data (Bressan et al. 2012), both stars are within reasonable errors of determination to the zero-age main sequence (ZAMS). If we adopt the higher temperature of Hubrig et al. (2001) to derive the photometric parallax from the formula

$$\log \Pi = 7.454 - \log R - 0.2V - 2F'_V, \qquad (1)$$

where the photometric fluxes (F'_V) are 4.024 and 4.021, respectively, using the bolometric corrections from Table 3.1 in Budding & Demircan (2007), the corresponding mean distance of the components is 112 pc. This is less than the *Hipparcos* distance, although the two values are within their probable errors of each other. The use of the empirical Barnes–Evans relation (Barnes & Evans 1976) with $V - R$ values derived from Table 2 gives larger F'_V values of 4.047 and 4.075 for the primary and secondary. The photometric parallaxes would then become 127 pc for the primary and 137 pc for the secondary. Our adopted model makes the secondary an atypical star, so the use of the Barnes–Evans relation is questionable in its case. The close agreement between the *Hipparcos* and photometric parallaxes for the primary, though, suggests that the photometric flux really is higher than that corresponding to the lower temperature of Section 2, so a better compromise is reached by the higher value in our finally adopted parameters in Table 7, with a 400-K decrement for the secondary.

5 OTHER COMPONENTS

5.1 η Mus B

The chemical peculiarity of η Mus B was mentioned in the Introduction. We present in Table 8 a listing of lines, mostly identified from the ILLSS and NIST catalogues (Coluzzi 1993, 1999; Ralchenko et al. 2011), as well as a few still unidentified features. The wavelengths given in Table 8 correspond to a predetermined Doppler shift of 14.5 km s^{-1}; however, the mean shift of the 479 lines is non-zero, implying a better estimate for the mean RV of η Mus B is 14.3 km s^{-2}. The difference between this value and the γ velocity of the close binary in 2006 was used by Bakış et al. (2007) as an argument for the unbound condition of the wide system η Mus AB; however, Butland & Budding (2011) showed that this γ velocity varies. The mean γ velocity turns out to be measurably the same as that of η Mus B, so we can attach more confidence to Tokovinin's (1997) appraisal of the wide system.

We examined a number of lines to assess the rotation of η Mus B, as in Section 3.1 for the close binary. Six clearly defined and symmetric lines selected for profile fittings were Fe II 6456, Si II 6371, Co I 5984, Fe I 4957, Mg I 4703, and Fe I 4525. The average projected equatorial rotation speed was found to be 31.7 ± 1.8. The convolved Gaussian component of the full line broadening was 22.5 ± 2.0.

5.2 η Mus C

If this star is bound to the bright close binary, as would seem likely given the bound nature of the much wider AB system, it must have orbital period in the order of 3000 yr. Although Hubrig et al. (2001) reported ∼10 mag (J), it was not resolved by 'lucky imaging' techniques in the V range (Idaczyk 2012).

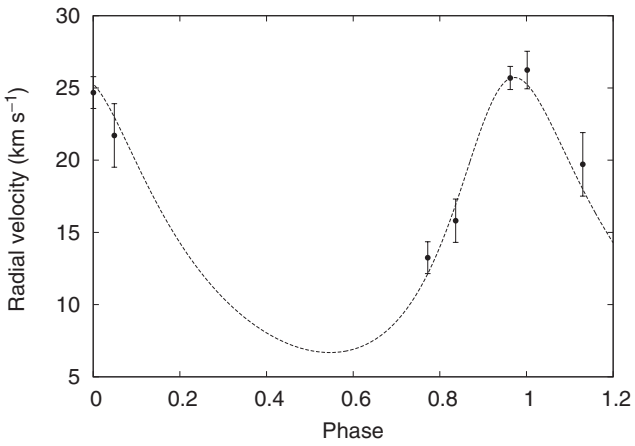

Figure 7. Preliminary orbital model fitting to observed variations of the γ velocity of η Mus.

5.3 η Mus D

A slight difference between the γ velocity applying to the RVs of 2006 May and September was noticed when the present authors re-analysed the spectra, and this prompted further observations since 2010. It became clear that the γ velocity of the main pair cycles on a relatively short timescale (∼5 yr), as shown in Figure 7.

The variations of γ velocity suggest observable effects in the time of minima, prompting further photometry. The model corresponding to Figures 7 and 8 yields a mass function of about 0.142. This would correspond to a third mass about 2.3 solar masses if the orbit were roughly coplanar with the central close pair. In turn, this would correspond to an A-type star about a couple of magnitudes fainter than either of the close binary stars, or about 6% of the system light. Such a third light contribution was considered in Section 2, but not identified. Since all the measured lines are associated with the B-type stars of the close pair, it seems unlikely that this new component would interfere with the RV model presented in Section 3, but this point should be examined further as the model for this wider orbit becomes better known.

5.4 Time of minimum variations

H. Hensberge (private communication, 2011) kindly forwarded the data they used to refine the mean orbital period of the close binary. These data are from patrol-type observations not specific to η Mus and so rather discontinuous. Here and there, the material becomes more bunched, however, and may include observations within eclipse minima. We sought to fit such data groups for timing variations, although derived shifts cannot have the same reliability as for completely covered eclipses.

We considered six main groups of data over the interval 1983–90, containing around a dozen points each. A set of 33 observations with greater scatter from early 1975 also sent by Dr Hensberge make up seven sparse light curves. In

Table 8. Spectrum measures for η Mus B

Measured	Reference	EW	Δλ	Species	Remark	Measured	Reference	EW	Δλ	Species	Remark
7165.15	7165.09	86	0.06	Si I		6176.947	6176.95	14	− 0.003	Cr II	b Fe II
7112.513	7112.53	46	− 0.017	Pr III		6175.091	6175.14	51	− 0.049	Fe II	
7076.918	7077.03	263	− 0.112	Ar II	b Eu II	6172.84	6172.91	43	− 0.07	Ti II	b La II
7056.306	7056.43	57	− 0.124	Tm II	id	6170.571	6170.568	67	0.003	Ni I	cgs
7030.395	7030.39	105	0.005	Pr III		6155.119	6155.24	77	− 0.121	Fe II	b
7004.986	7004.81	341	0.176	Co I	b id	6147.642	6147.735	75	− 0.093	FeII	
6855.194	6855.176	59	0.018	Fe I		6145.049	6145.08	131	− 0.031	SiI	b Nd III
6841.593	6841.65	37	− 0.057	Fe I		6142.058	6142.047	91	0.011	NiI	
6838.766	6838.86	20	− 0.094	Fe I		6131.502	6131.54	43	− 0.038	SiI	cd
6832.854	6832.93	16	− 0.076	Zr I		6129.2	6129.23	54	− 0.03	CrII	b Mn II
6828.371	6828.25	95	0.121	Gd I	id	6113.182	6113.33	59	− 0.148	Fe II	b
6793.617	6793.62	53	− 0.003	Fe I		6106.268	6106.19	55	0.078	GdII	
6780.475	6780.51	23	− 0.035	Ge II	id	6102.748	6102.722	115	0.026	CaI	
6774.239	6774.26	17	− 0.021	La II		6093.889	6093.935	42	− 0.046	CeII	
6768.409	6768.65	19	− 0.241	Ti I	id	6089.853	6089.69	118	0.163	Cr II	b Hg II
6757.557	6757.78	30	− 0.223	Cr I		6084.118	6084.11	44	0.008	FeII	
6748.797	6748.79	24	0.007	S I		6078.627	6078.496	51	0.131	Fe I	id b
6744.337	6744.38	28	− 0.043	C III	id	6069.788	6069.69	26	0.098	Cr II	
6737.944	6737.9848	23	− 0.0408	Fe I		6067.798	6067.88	28	− 0.082	Cr I	
6727.309	6727.6	70	− 0.291	Fe II	b	6065.47	6065.487	27	− 0.017	Fe I	cgs
6721.8	6721.89	41	− 0.09	Fe I		6060.931	6060.925	43	0.006	Fe I	b
6706.76	6706.705	66	0.055	Pr III		6053.03	6053.01	162	0.02	Pr III	
6690.838	6690.8	36	0.038	Ni I		6049.548	6049.5	60	0.048	Gd II	b Eu II
6677.913	6677.99	135	− 0.077	Fe I	b	6045.373	6045.497	45	− 0.124	Fe II	b
6666.22	6666.36	23	− 0.14	Ar II ?	id	6024.022	6024.066	69	− 0.044	Fe I	cgs
6644.965	6644.96	114	0.005	N I		6020.118	6020.1688	46	− 0.0508	Fe I	
6633.846	6633.764	26	0.082	Fe I		6012.359	6012.4373	34	− 0.0783	Fe I	
6627.362	6627.28	39	0.082	Fe II		6008.299	6008.35	69	− 0.051	Fe I	b Mn II
6622.233	6622.28	16	− 0.047	Gd II		5998.674	5998.61	147	0.064	Ni I	b
6616.489	6616.46	45	0.029	Pr III		5991.361	5991.383	71	− 0.022	Fe II	b Fe I
6613.69	6613.62	57	0.07	N II	b Fe I	5987.636	5987.85	179	− 0.214	Gd III	id b
6608.884	6608.952	35	− 0.068	Fe I		5984.249	5984.253	124	− 0.004	Co I	cd
6604.501	6604.6	41	− 0.099	Sc II	b Sm II	5978.849	5978.97	132	− 0.121	Si II	b hs
6562.819	6562.817		0.002	H alf		5965.844	5965.828	43	0.016	Ti I	
6550.211	6550.244	157	− 0.033	Sr I		5957.432	5957.612	57	− 0.18	Si II	id
6526.789	6526.85	63	− 0.061	Si I		5955.985	5956.05	91	− 0.065	Pr III	
6516.047	6516.053	163	− 0.006	Fe II		5952.538	5952.55	54	− 0.012	Fe II	
6501.188	6501.212	82	− 0.024	Cr I		5948.351	5948.3	116	0.051	La II	
6456.404	6456.376	242	0.028	Fe II		5952.5	5952.55	58	− 0.05	Fe II	
6443.055	6443.05	32	0.005	La II	b	5948.354	5948.3	136	0.054	La II	b Si I
6438.1	6438.172	86	− 0.072	Cs II	id	5941.014	5940.972	128	0.042	Fe I	
6417.056	6416.94	162	0.116	Fe I		5935.022	5935.129	43	− 0.107	Fe I	id
6411.596	6411.658	70	− 0.062	Fe I	cgs	5930.1	5930.173	73	− 0.073	Fe I	
6407.689	6407.675	118	0.014	N I	id	5914.083	5914.16	127	− 0.077	Fe I	
6399.954	6400.01	112	− 0.056	Fe I	cgs	5903.395	5903.317	93	0.078	Ti I	
6393.583	6393.605	70	− 0.022	Fe I		5889.964	5889.9953	177	− 0.0313	Na I	
6385.339	6385.196	52	0.143	Nd II	b Fe II	5867.015	5867.01	17	0.005	Fe I	
6371.333	6371.359	182	− 0.026	Si II		5862.401	5862.3561	47	0.0449	Fe I	
6361.519	6361.65	66	− 0.131	Pr III		5859.707	5859.608	41	0.099	Fe I	b
6347.027	6347.091	246	− 0.064	Si II		5851.793	5851.758	254	0.035	Hg II	
6336.26	6336.34	53	− 0.08	Gd I	b Ti I	5844.91	5844.88	189	0.03	Fe I	b
6332.013	6331.969	63	0.044	Fe II		5842.121	5842.027	46	0.094	Fe I	b Hf II
6327.298	6327.21	142	0.088	Sc I	id	5826.544	5826.638	66	− 0.094	Fe I	
6317.957	6318.022	91	− 0.065	Fe I		5816.367	5816.36	55	0.007	Fe I	
6254.349	6254.262	83	0.087	Fe I	cgs	5813.595	5813.67	37	− 0.075	Fe II	b
6247.537	6247.562	144	− 0.025	Fe II		5809.519	5813.5	36	− 3.981	Hf II	b Fe II
6243.82	6243.813	51	0.007	Si I		5806.821	5806.75	51	0.071	Si II	
6238.569	6238.5	381	0.069	Nd II	b Fe II	5802.53	5802.67	113	− 0.14	Mo I	id b
6195.52	6195.63	133	− 0.11	Pr III		5797.347	5797.352	65	− 0.005	V I	b Ti I
6191.649	6191.562	58	0.087	Fe I	b Fe II	5790.961	5791	88	− 0.039	Cr I	
6188.224	6188.037	29	0.187	Fe I	b	5783.88	5783.934	119	− 0.054	Cr I	cgs
6185.882	6185.697	33	0.185	Fe I	id	5780.185	5780.189	55	− 0.004	Mn I	

Table 8. Contd.

Measured	Reference	EW	Δλ	Species	Remark	Measured	Reference	EW	Δλ	Species	Remark
6179.213	6179.17	42	0.043	Cr II		5775.412	5775.4	50	0.012	Lu I	
5772.116	5772.145	25	− 0.029	Si II		5487.641	5487.747	120	− 0.106	Fe I	b
5762.962	5762.9918	83	− 0.0298	Fe I	cgs	5478.349	5478.35	43	− 0.001	Cr II	
5753.346	5753.38	100	− 0.034	Fe I		5476.508	5476.571	68	− 0.063	Fe I	
5747.81	5747.85	69	− 0.04	Fe I	b Fe II	5472.629	5472.63	125	− 0.001	Cr II	
5741.258	5741.22	54	0.038	Ti I		5466.478	5466.46	195	0.018	Fe I	b Y I
5733.731	5733.86	26	− 0.129	Gd II		5463.132	5463.282	154	− 0.15	Fe I	cs
5726.546	5726.83	32	− 0.284	Nd II		5455.632	5455.613	204	0.019	Fe I	hs
5718.244	5718.12	53	0.124	Nd II		5445.061	5445.045	60	0.016	Fe I	cgs
5714.329	5714.5487	50	− 0.2197	Fe I	id	5432.86	5432.95	139	− 0.09	Fe I	
5708.696	5708.639	127	0.057	Sc I		5429.741	5429.699	254	0.042	Fe I	hs
5708.711	5708.89	124	− 0.179	Zr I	b Fe I	5425.377	5425.29	38	0.087	Cr II	b Fe II hs
5705.688	5705.48	98	0.208	Fe I	id	5424.05	5424.072	97	− 0.022	Fe I	hs
5701.837	5701.898	79	− 0.061	Fe I		5420.988	5420.9	100	0.088	Cr II	
5698.429	5698.3645	43	0.0645	Fe I	cgs	5414.771	5414.63	278	0.141	Er II	id b Fe I
5695.127	5695.0916	34	0.0354	Pd I	id	5409.99	5409.791	409	0.199	Cr I	b cgs
5684.326	5684.24	43	0.086	Eu I	b Sc II	5407.586	5407.62	51	− 0.034	Cr II	
5680.921	5680.93	25	− 0.009	Zr I		5405.73	5405.778	127	− 0.048	Fe I	cs
5677.161	5677.03	75	0.131	Pr II	id b	5404.124	5404.144	120	− 0.02	Fe I	cgs
5671.515	5671.54	40	− 0.025	La II	cgs	5400.491	5400.509	104	− 0.018	Fe I	
5669.038	5669.03	54	0.008	Sc II		5397.608	5397.6	157	0.008	Fe I	hs cgs
5666.912	5666.837	29	0.075	Fe I		5393.357	5393.174	89	0.183	Fe I	b cgs
5662.797	5662.94	82	− 0.143	Fe I	b Ti I	5391.109	5391.06	52	0.049	Ti I	
5658.451	5658.531	165	− 0.08	Fe I	b	5386.896	5386.958	89	− 0.062	Fe I	
5655.118	5655.1761	167	− 0.0581	Fe I		5383.392	5383.374	108	0.018	Fe I	cgs
5645.256	5645.399	78	− 0.143	Fe II	id	5379.25	5379.19	46	0.06	Ti II	
5637.703	5637.734	77	− 0.031	Co I		5377.629	5377.63	26	− 0.001	Mn I	
5633.635	5633.97	137	− 0.335	Fe I	id b	5371.536	5371.493	114	0.043	Fe I	cs
5627.412	5627.49	36	− 0.078	Fe II		5369.921	5369.965	145	− 0.044	Fe I	cgs
5624.517	5624.549	94	− 0.032	Fe I	cgs	5367.581	5367.47	63	0.111	Fe I	b cgs
5620.605	5620.62	75	− 0.015	Nd II	b Cr II	5364.94	5364.874	93	0.066	Fe I	cgs
5615.609	5615.652	144	− 0.043	Fe I	cgs	5362.86	5362.864	173	− 0.004	Fe II	
5610.247	5610.257	45	− 0.01	Ce II	id	5353.394	5353.3732	39	0.0208	Fe I	
5602.81	5602.846	73	− 0.036	Ca I	cs	5348.205	5348.32	24	− 0.115	Cr I	cgs
5600.754	5600.66	60	0.094	Fe II		5345.878	5345.81	147	0.068	Cr I	cgs
5598.161	5598.163	83	− 0.002	Sr I	b Fe I	5340.032	5340.02	269	0.012	Pr III	b Fe I
5602.873	5602.846	75	0.027	Ca I	cs	5334.744	5334.7	58	0.044	Al VI	b Mn I
5600.717	5600.66	53	0.057	Fe II		5332.88	5332.8894	30	− 0.0094	Fe I	
5598.132	5598.163	77	− 0.031	Sr I	id	5328.432	5328.34	399	0.092	Cr I	b Fe I
5594.616	5594.661	69	− 0.045	Fe I	b Co I	5325.587	5325.553	87	0.034	Fe II	hs cgs
5586.752	5586.763	182	− 0.011	Fe I	cgs	5324.197	5324.1787	77	0.0183	Fe I	
5581.674	5581.74	51	− 0.066	Pr III		5316.624	5316.615	289	0.009	Fe II	hs cgs
5572.949	5572.849	166	0.1	Fe I		5313.469	5313.563	102	− 0.094	Cr II	
5569.548	5569.625	122	− 0.077	Fe I	cgs	5310.595	5310.7	85	− 0.105	Cr II	
5567.807	5567.815	25	− 0.008	Fe II		5308.434	5308.44	90	− 0.006	Cr II	
5565.875	5565.708	110	0.167	Fe I	id	5305.934	5305.85	116	0.084	Cr II	
5563.499	5563.604	35	− 0.105	Fe I		5302.6	5302.62	200	− 0.02	La II	
5554.888	5554.895	53	− 0.007	Fe I		5299.911	5299.9	85	0.011	Fe III	b Pr III
5543.776	5543.86	171	− 0.084	Cr II		5294.086	5293.973	125	0.113	Fe I	b Nd III
5543.719	5543.86	207	− 0.141	Cr II	b c	5286.752	5286.74	78	0.012	Fe III	b
5534.885	5534.86	182	0.025	Fe II	hds	5284.199	5284.109	421	0.09	Fe II	b
5530.807	5530.78	63	0.027	Co I		5281.801	5281.796	108	0.005	Fe I	cgs
5528.34	5528.3876	83	− 0.0476	Mg I	hds	5279.955	5279.92	124	0.035	Cr II	
5525.24	5525.14	44	0.1	Fe II		5275.605	5275.689	339	− 0.084	Cr I	b Fe I
5521.404	5521.44	91	− 0.036	Ni I	b	5273.459	5273.431	47	0.028	Nd II	
5510.65	5510.58	67	0.07	Gd II	b Cr II	5269.8	5269.86	255	− 0.06	Pu I	b Ti I
5508.577	5508.606	35	− 0.029	Cr II		5266.589	5266.562	153	0.027	Fe I	cs
5506.239	5506.196	155	0.043	Fe II		5264.603	5264.44	428	0.163	Pr III	b Fe II
5502.76	5502.88	244	− 0.12	Al II	b	5261.727	5261.706	36	0.021	Ca I	cs
5497.586	5497.519	130	0.067	Fe I	cgs	5260.064	5259.976	126	0.088	Ti I	
5493.833	5493.85	71	− 0.017	Fe I		5256.969	5256.89	65	0.079	Fe II	
5487.607	5487.52	111	0.087	Fe I	b	5255.021	5254.956	163	0.065	Fe I	cgs

Table 8. Contd.

Measured	Reference	EW	Δλ	Species	Remark	Measured	Reference	EW	Δλ	Species	Remark
5497.584	5497.519	110	0.065	Fe I	cgs	5249.436	5249.437	62	− 0.001	Cr II	
5493.819	5493.85	52	− 0.031	Fe I		5243.306	5243.31	124	− 0.004	Fe III	
5239.751	5239.79	51	− 0.039	Nd II		5048.132	5048.082	59	0.05	Ni I	b
5237.48	5237.43	149	0.05	Nb I	b Cr II	5043.912	5043.86	43	0.052	Er I	id
5234.567	5234.62	147	− 0.053	Fe II		5041.105	5041.074	275	0.031	Fe I	cgs
5232.779	5232.946	200	− 0.167	Fe I	id	5035.774	5035.773	56	0.001	Fe II	
5227.048	5227.1	299	− 0.052	Cr I	b	5030.922	5031.03	90	− 0.108	Fe I	
5215.989	5215.928	281	0.061	V II	b	5027.569	5027.51	198	0.059	Fe I	b
5210.733	5210.5672	98	0.1658	Ne I	b Co I	5024.707	5024.7933	51	− 0.0863	Fe I	b Ti I
5208.448	5208.436	271	0.012	Cr I	cgs	5022.384	5022.244	148	0.14	Fe I	cgs
5206.057	5206.039	121	0.018	Cr I	cgs	5018.451	5018.434	246	0.017	Fe II	hs
5204.098	5204.14	263	− 0.042	La II		5014.952	5014.95	69	0.002	Fe I	
5202.37	5202.339	80	0.031	Fe I		5012.995	5012.957	96	0.038	Ba II	id
5197.589	5197.569	95	0.02	Fe II	b Gd II	5010.347	5010.3	25	0.047	Fe I	
5195.415	5195.471	194	− 0.056	Fe I		5005.951	5006.059	134	− 0.108	Si I	b Fe I cgs
5192.869	5192.75	127	0.119	Ti II	b Si II	5004.184	5004.034	71	0.15	Fe I	b Co I
5188.746	5188.7	42	0.046	Ti II		5001.87	5001.871	142	− 0.001	Fe I	b Zr II
5191.486	5191.448	79	0.038	Nd II		4993.425	4993.355	102	0.07	Fe II	
5187.34	5187.237	50	0.103	Gd II		4991.121	4991.11	93	0.011	Fe II	
5185.811	5185.7257	62	0.0853	Fe I	b Ti II	4988.969	4988.963	36	0.006	Fe I	
5183.571	5183.6042	286	− 0.0332	Mg I		4985.386	4985.261	54	0.125	Fe I	cgs
5177.431	5177.43	31	0.001	Cr I		4983.871	4983.855	63	0.016	Fe I	cgs
5172.725	5172.6843	165	0.0407	Mg I		4982.493	4982.507	57	− 0.014	Fe I	cgs
5169.052	5169.03	331	0.022	Fe II	hs cgs	4978.47	4978.606	18	− 0.136	Fe I	cgs
5167.401	5167.491	170	− 0.09	Fe I	b Mg I	4973.061	4973.051	58	0.01	Ti I	
5165.366	5165.422	45	− 0.056	Fe I		4970.366	4970.39	90	− 0.024	La II	
5162.363	5162.38	74	− 0.017	Fe I		4967.978	4967.944	44	0.034	Sr I	b Fe I
5160.821	5160.896	47	− 0.075	Gd II		4966.125	4966.096	31	0.029	Fe I	b V II
5158.902	5158.854	33	0.048	Co I	b Fe II	4964.524	4964.713	43	− 0.189	Ti I	id
5154.187	5154.28	192	− 0.093	Cr I	b Fe II	4962.014	4962.1	71	− 0.086	Al II	
5151.81	5151.83	121	− 0.02	Cr I		4957.495	4957.453	298	0.042	Fe I	b cs
5149.431	5149.538	32	− 0.107	Fe II		4948.574	4948.617	57	− 0.043	Sm II	b
5148.146	5148.234	75	− 0.088	Fe I		4946.31	4946.394	39	− 0.084	Fe I	cgs
5146.036	5146.12	26	− 0.084	Fe II		4942.649	4942.59	190	0.059	Fe I	b Cr I
5144.359	5144.413	40	− 0.054	Al II	b Fe II	4938.848	4938.82	170	0.028	Fe I	
5142.491	5142.541	51	− 0.05	Fe I		4936.207	4936.155	44	0.052	Gd II	
5139.39	5139.468	172	− 0.078	Fe I	b cgs	4933.808	4933.878	101	− 0.07	Fe I	
5137.217	5137.388	114	− 0.171	Fe I		4927.501	4927.42	153	0.081	Fe I	
5133.788	5133.692	115	0.096	Fe I	cgs	4923.923	4923.921	289	0.002	Fe II	hs
5130.538	5130.596	24	− 0.058	Nd II		4920.658	4920.692	281	− 0.034	Nd II	b Fe I
5127.136	5127.09	191	0.046	Cr II	b Fe I cgs	4919.027	4918.999	109	0.028	Fe I	cgs
5125.147	5125.13	73	0.017	Fe I		4922.219	4922.18	29	0.039	Fe I	
5123.381	5123.465	79	− 0.084	Cr I	cgs	4914.2	4914.2382	44	− 0.0382	Cs II	b
5119.338	5119.47	28	− 0.132	Cr II	b	4912.911	4912.82	86	0.091	Ca I	
5116.982	5117.0072	58	− 0.0252	Pd I	id b	4903.291	4903.239	152	0.052	Cr I	
5110.195	5110.36	97	− 0.165	Fe I	id b	4901.666	4901.65	79	0.016	Cr II	
5107.529	5107.64	88	− 0.111	Fe I	cgs	4900.093	4900.03	88	0.063	Ti I	b
5102.476	5102.39	188	0.086	Nd II	id b Fe I	4893.978	4893.9	73	0.078	Ti I	b Fe II
5100.748	5100.704	138	0.044	Fe II	b cgs	4891.131	4891.07	364	0.061	Nd I	b La II
5098.757	5098.703	56	0.054	Fe I		4888.743	4888.6366	95	0.1064	Fe I	
5097.158	5096.998	147	0.16	Fe I	id	4884.73	4884.57	20	0.16	Cr II	
5093.488	5093.47	50	0.018	Fe II		4883.988	4883.9	16	0.088	Fe III	
5090.781	5090.787	51	− 0.006	Fe I		4878.19	4878.132	76	0.058	Ca I	b Fe I
5087.527	5087.42	53	0.107	Y II	b Fe II	4876.353	4876.325	97	0.028	Sr I	
5084.993	5085.02	71	− 0.027	Al II		4871.296	4871.27	113	0.026	Fe II	b Fe I
5082.111	5082.074	21	0.037	Ce II	b Ni I	4886.774	4886.725	72	0.049	Ni I	
5079.088	5079.002	119	0.086	Fe I	b	4881.926	4881.925	61	0.001	Gd II	
5075.497	5075.35	273	0.147	Ce II	id	4872.29	4872.14	20	0.15	Fe I	id b
5072.432	5072.4	79	0.032	Fe II		4861.284	4861.332		− 0.048	H beta	
5068.85	5068.774	63	0.076	Fe I	cgs	4848.24	4848.24	96	0	Cr II	
5064.912	5064.95	153	− 0.038	Fe I		4839.926	4840	38	− 0.074	Fe II	
5061.666	5061.794	47	− 0.128	Fe II	id	4836.179	4836.18	104	− 0.001	Cr I	b Ti I

Table 8. Contd.

Measured	Reference	EW	Δλ	Species	Remark	Measured	Reference	EW	Δλ	Species	Remark
5059.538	5059.48	61	0.058	Pt I	id	4829.321	4829.376	53	− 0.055	Cr I	b Sm II
5056.062	5056	264	0.062	Fe I	b Si II	4825.376	4825.46	16	− 0.084	Ti I	
5050.48	5050.57	167	− 0.09	La I	b Fe I	4823.876	4823.84	230	0.036	P II	id b
4821.998	4821.955	22	0.043	Gd II		4656.97	4656.981	130	− 0.011	Fe II	
4815.851	4815.808	38	0.043	Sm II		4654.353	4654.32	226	0.033	Si IV	b Fe I
4812.296	4812.24	66	0.056	Ti I		4647.73	4647.72	29	0.01	Fe I	
4810.427	4810.299	80	0.128	N II	id b	4646.239	4646.174	104	0.065	Cr I	cs
4804.994	4805.105	101	− 0.111	Ti II	hs	4635.507	4635.539	72	− 0.032	Ti I	
4802.764	4802.881	23	− 0.117	Fe I	b	4634.003	4633.99	83	0.013	Zr I	b Cr II
4800.998	4801.03	34	− 0.032	Cr I	b Gd II	4640.82	4640.735	36	0.085	V I	b Cr I
4799.822	4799.859	50	− 0.037	Gd II	b Ni I	4635.287	4635.328	57	− 0.041	Fe II	
4794.371	4794.36	27	0.011	Fe I		4631.944	4631.93	16	0.014	Fe I	
4789.496	4789.41	39	0.086	Nd II	b Cr I	4629.332	4629.336	79	− 0.004	Fe II	hs
4788.34	4788.36	25	− 0.02	Li II		4625.033	4625.052	49	− 0.019	Fe I	b Cr I cgs
4786.687	4786.61	106	0.077	Yb II	b Fe I	4620.57	4620.513	71	0.057	Fe II	
4783.233	4783.306	123	− 0.073	Ti I	b Mn I	4618.883	4618.83	172	0.053	Cr II	hs
4777.651	4777.68	15	− 0.029	Fe III		4616.37	4616.389	260	− 0.019	Cr I	c Cr II
4771.197	4771.101	87	0.096	Ti I	b Co I	4613.272	4613.21	51	0.062	Fe I	hs
4762.524	4762.376	47	0.148	Mn I	b cgs	4611.354	4611.35	103	0.004	Fe I	
4761.328	4761.42	24	− 0.092	Cr II		4607.595	4607.655	75	− 0.06	Fe I	
4759.593	4759.65	121	− 0.057	Er II	b Cr I	4602.853	4602.944	22	− 0.091	Fe I	cs
4757.568	4757.591	44	− 0.023	Cr I	b Fe I	4595.515	4595.59	69	− 0.075	Cr I	
4755.882	4755.728	58	0.154	Mn II	id	4604.348	4604.42	37	− 0.072	Zr I	b Fe II
4752.034	4752.084	36	− 0.05	Cr I		4601.026	4601.021	78	0.005	Cr I	cs
4745.803	4745.806	69	− 0.003	Fe I		4598.039	4598.07	97	− 0.031	Fe II	
4736.949	4737	123	− 0.051	C IV	b	4595.583	4595.59	118	− 0.007	Cr I	b Fe II
4731.451	4731.439	160	0.012	Fe II	hs	4593.785	4593.84	64	− 0.055	Cr I	b Sm II
4727.652	4727.476	103	0.176	Mn I	id	4592.001	4592.09	200	− 0.089	Cr II	
4723.075	4723.06	87	0.015	Cr I		4589.863	4589.89	107	− 0.027	Cr II	
4713.502	4713.5	108	0.002	Nb I	b He I	4588.241	4588.217	156	0.024	Cr II	hs
4718.157	4718.16	115	− 0.003	Ca II	b Sm II	4583.958	4583.99	160	− 0.032	Fe II	hs
4715.13	4715.21	17	− 0.08	Fe I	b Ti I cgs	4582.693	4582.835	98	− 0.142	Fe II	hs
4709.279	4709.336	19	− 0.057	Sc I		4579.804	4579.825	107	− 0.021	Fe I	
4707.555	4707.541	105	0.014	Pr II		4576.332	4576.331	153	0.001	Fe II	
4702.968	4702.9758	101	− 0.0078	Mg I	hs	4565.673	4565.684	91	− 0.011	Fe I	
4699.468	4699.589	40	− 0.121	Cr I	b	4563.74	4563.761	98	− 0.021	Ti II	
4698.457	4698.466	35	− 0.009	Cr I		4558.61	4558.659	191	− 0.049	Cr II	hs cgs
4697.339	4697.393	24	− 0.054	Cr I	cgs	4556.019	4556.06	126	− 0.041	Pm I	b Fe II
4695.321	4695.363	60	− 0.042	Ne I	id	4554.953	4554.989	69	− 0.036	Gd II	
4693.399	4693.56	102	− 0.161	Fe I	b	4552.473	4552.453	28	0.02	Ti I	cs
4691.476	4691.55	36	− 0.074	Fe II		4551.05	4550.954	72	0.096	Gd II	
4689.115	4689.07	98	0.045	U II	id	4549.489	4549.467	314	0.022	Fe II	hs
4684.676	4684.605	54	0.071	Cr I	b Ce II	4541.479	4541.513	74	− 0.034	Cr I	b Fe II
4682.396	4682.374	58	0.022	Co I		4539.653	4539.62	72	0.033	Cr II	
4680.498	4680.49	30	0.008	Cr I	b Fe I	4535.537	4535.574	30	− 0.037	Ti I	cs
4678.78	4678.821	87	− 0.041	Fe I		4534.09	4533.966	140	0.124	Ti II	hs
4672.707	4672.83	46	− 0.123	Fe I	id	4530.787	4530.755	39	0.032	Cr I	d
4670.348	4670.404	22	− 0.056	Sc II	hs	4525.046	4525.142	73	− 0.096	Fe I	b
4669.308	4669.336	49	− 0.028	Cr I	b Sm II	4522.621	4522.634	235	− 0.013	Fe II	hs
4666.748	4666.75	138	− 0.002	Fe II	hs	4520.128	4520.225	147	− 0.097	Fe II	hs
4663.643	4663.7	64	− 0.057	Fe II							

The measured wavelengths are shown with an *ad hoc* correction of 14.5 km s^{-1} to give closeness to the (air) reference values. The differences between these two (Δλ) are listed in the fourth column. Equivalent widths (EW) are given in units of mÅ of the local continuum. The fifth column identifies the expected source atom or ion, usually on the basis of wavelength proximity. The remarks correspond to—b: a blend, often with an expected close feature named; sometimes not, in the case of various possibilities; id: uncertainty of identification; cs: a well-known feature of cool stellar spectra, or cgs: associated more with a low gravity cool atmosphere; hs: a feature expected in normal dwarf stellar spectra of type earlier than A4. The data from which this table was composed can be made available to any interested specialist.

Table 9. $O - C$ data for η Mus

	Epoch (245+)		
Eclipse type	Observed	Calculated	$O - C$
p	3974.9159 ± 0.0010	3974.91600	− 0.00010
s	3992.8900 ± 0.0009	3992.88837	0.00163
s	5723.0258 ± 0.0009	5723.02859	− 0.00280
p	5776.9450 ± 0.0036	5776.94571	− 0.00068
s	6020.1758 ± 0.0010	6020.17179	0.00403
s	6056.1232 ± 0.0006	6056.11653	0.00669
p	6086.0757 ± 0.0006	6086.07048	0.00518

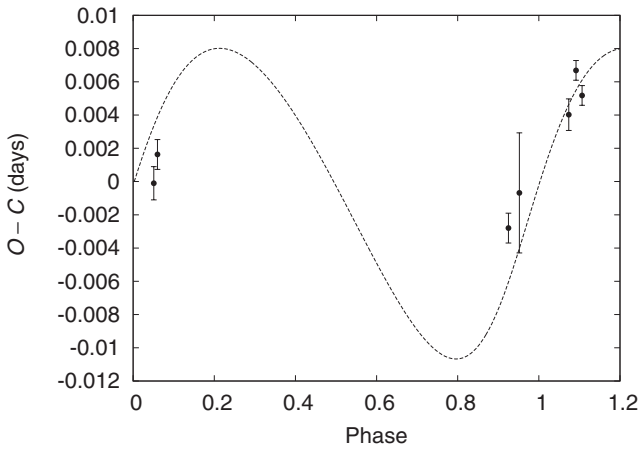

Figure 8. Measured $O - C$ from times of minima of η Mus A due to η Mus D. The calculated light travel time derived from the γ velocity fitting in Figure 7 is also shown.

testing these data sets, we assumed the light curve model corresponding to the parameters of Table 2 and allowed only the zero point of the phases ($\Delta\phi_0$) and system luminosity ('unit of light') to vary. The scale of $O - C$ differences found was generally consistent with their expected range (~0.01 d), but with an appreciable scatter. Unfortunately, these findings were too few and from essentially too small data sets to be convincing.

On the other hand, more consistency has been found between the spectrometry-derived third orbit and recent determinations of times of minima from full eclipse coverage using DSLR techniques. Preliminary findings were reported by Idaczyk (2012) and are shown in Table 9 and Figure 8, where we include points from Bakış et al. (2007), as well as our own observations. A fuller tally of results will be published in due course.

6 DISCUSSION

The RV amplitudes and masses given in Table 7 are not significantly different from those given by Bakış et al. (2007). There are, however, at least two major differences of interpretation between Bakış et al. (2007) and the present study. We dealt already with one of these in Section 5, namely that the visual companion η Mus B does have a real physical connection to the close binary, even though their mean RVs may sometimes appear different by several times greater than the error of the determination. Bakış et al. confirmed the likely membership of η Mus B to the LCC concentration of the Sco–Cen OB2 association, though their argument cast doubt on that of η Mus A. The inner A–D orbit now supports the inference of a common origin for the multiple star.

The other difference arises from the confirmed result that the secondary has a higher projected rotation speed than the primary. Our findings support those of Bakış et al. (2007), although we claim this result does not have a very high precision. Our use of the IRAF profile fitter on 65 line pairs produced an appreciable scatter in widths for many of the lines, but we should note that maximum depths are still only a few percent of the continuum. Our adopted results in Table 7 give that the secondary star is larger than the primary, though it must be cooler to account for the difference in depths of the two eclipses. At the same time, the masses of the two stars are essentially the same to within measurement errors. As with Bakış et al. (2007), we assign a slightly smaller mass to the secondary star. Keeping in mind the normal relation of mass and radius for MS stars, how then does it come to be larger?

Our interpretation of this point is based on models of very young stars, still in the process of arrival at the ZAMS (Siess, Dufour, & Forestini 2000). The irregular episodes of enhanced luminosity during the final descent to the ZAMS are sometimes associated with the 'deuterium flash', though the word flash may be somewhat misleading for time intervals of several hundreds of thousands of years. Recent tabulated data from the CMD webpage (Bressan et al. 2012) used to make isochrones can be easily adapted to show radius versus time, since luminosities and effective temperatures are listed for given masses over specifiable age ranges, including PMS stages. The final condensation to the MS stage seen at the left of Figure 9 shows that there can be an appreciable interval of time (of the order of a few $\times 0.1$ Myr) during which a less massive star would be significantly larger than the more massive one.

An alternative scenario in which the putative secondary is slightly more massive than its partner could be thought of. The difference in its radius might then be associated with a pair of similar stars approaching the end of their MS stage. At some point, the relatively rapid growth of the more massive star could then allow for the obtained ratio of radii to be realised. However, checks of stellar evolution tracks for stars of mass around 3.3 $M_\odot$ (Figure 9 and Bertelli et al. 2009) show that by the time this might occur, given the very small mass differential, both stars would have to become significantly larger than the radii given in Table 7.

Overall, our picture of the η Mus multiple star, in not requiring a recent close encounter with an unidentified passing object, appears simpler and more direct than the account of

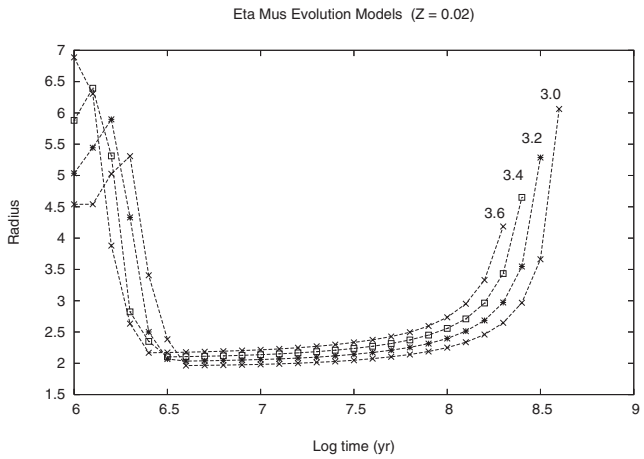

Figure 9. The evolution of stellar radii (solar units) derived from the data of Bressan et al. (2012) for stars of 3.0–3.6 solar masses, as indicated. Component radii can be seen to grow appreciably larger than those of Table 7 before the relatively rapid expansion away from the MS at the right.

Bakış et al. (2007), but a number of intriguing points remain. How did this very young stellar system arrive in the configuration found? The inferred young age contrasts with the Sartori, Lépine, & Dias (2003) 16–20 Myr age for stars selected from the Sco–Cen OB association, although characterising all the stars in this very large association by a narrow range can be questioned while ongoing star formation has been identified within it (Preibisch & Mamajek 2008). Paper II's study of the comparable system V831 Cen produced an age within the range of Sartori et al. (2003), but essentially the same procedures have led to the much younger result for η Mus. We can also ask about the Ap nature of η Mus B, noting also the similar condition of the third star in the comparable system V831 Cen. All such questions, as well as the atypical binary configuration, call for continued observations of the intriguing η Mus multiple star.

7 CONCLUSIONS

The Sco–Cen complex is an important astrophysical laboratory for studies of recently formed stars. Close binary or multiple systems, especially if eclipses are present, represent a small but highly significant subgroup within this population, whereby hard evidence on stellar masses, luminosities, and composition can be quantified. It is also important that such evidence continues to be gathered, carefully checked and, where possible, counterchecked by alternative groups, methods, and technologies.

Our challenge to inferences about the complete system previously made by Bakış et al. (2007) are underpinned, to a large extent, by our finding that η Mus B is gravitationally bound to the close binary. This relates to the recent discovery of η Mus D, and our new photometric and spectroscopic data about this.

Our absolute parameters, especially the stellar radii, argue for a young age, i.e. that the secondary of η Mus A is still condensing to the MS, so that its unexpectedly high rotation speed is due to its greater size; and that neither it nor the primary is asynchronously rotating, but their rotation speeds are consistent with tidal locking. These claims invite still more detailed observational checks and future research. η Mus thus appears a special case to test stellar modelling theory, given the precise age determination we infer.

ACKNOWLEDGEMENTS

We acknowledge useful input from Professors O. Demircan and A. Erdem as well as research students and staff of the Department of Physics, 18th March University of Çanakkale, Turkey. Many of the original set of spectrograms studied in this paper were gathered by V. Bakış and H. Bakış during the period of study in New Zealand in 2006 that was supported by the Science Research Council of Turkey (TÜBİTAK).

Generous allocations of time on the 1-m McLennnan Telescope and the HERCULES spectrograph at the Mt John University Observatory supporting the Southern Binaries Programme have been made available through its TAC and Director, Dr K. Pollard, and previous Director, Prof J. B. Hearnshaw. Useful assistance was provided by the MJUO management (A. Gilmore and P. Kilmartin). Considerable help with the use and development of the HRSP software (leading up to the latest version 5) was given by its author Dr J. Skuljan. Besides HRSP, the user-friendly freeware IMAGEJ was found useful for preliminary image checks. We are also grateful to Matthew Davie of UoC's Department of Physics and Astronomy for new spectroscopic data on η Mus.

Encouragement and support for this program has been shown by the Carter Observatory and the School of Chemical and Physical Sciences of the Victoria University of Wellington, as well as the Royal Astronomical Society of New Zealand and its Variable Stars South section (http://www.variablestarssouth.org). We thank VSS Director Tom Richards for advocating DSLR photometry in support of this program.

REFERENCES

Bakış, V., Bakış, H., Eker, Z., & Demircan, O. 2007, MNRAS, 382, 609
Banks, T., & Budding, E. 1990, Ap&SS, 167, 221
Barnes, J. 1993, BAAS, 25, 1435
Barnes, T. G., & Evans, D. S. 1976, MNRAS, 174, 489
Bertelli, G., Nasi, E., Girardi, L., & Marigo, P. 2009, A&A, 508, 355
Bidelman, W. P., & McConnell, D. J. 1973, AJ, 78, 687
Blaauw, A. 1964, IAUS, 29, 23
Blackford, M. G., & Schrader, G., 2011, VSS Newsl., 2, 8
Bressan, A., Marigo, P., Girardi, L., Salasnich, B., Dal Cero, C., Rubele, S., & Nanni, A. 2012, MNRAS, 427, 127
Budding, E. 2008, in APRIM 2008: Proceedings of the 10th Asian-Pacific Regional IAU Meeting Kunming, China, August 3–6, ed.

S. N. Zhang, Y. Li, & Q. J. Yu (China: National Observatories of China Press, 33
Budding, E., & Demircan, O. 2007, An Introduction to Astronomical Photometry (Cambridge, UK: Cambridge University Press)
Budding, E., Erdem, A., İnlek, G., & Demircan, O. 2010, MNRAS, 403, 1448
Budding, E., İnlek, G., & Demircan, O. 2009, MNRAS, 393, 501
Butland, R., & Budding, E. 2011, IBVS, 6004
Coluzzi, R. 1993, BICDS, 43, 7
Coluzzi, R. 1999, VizieR On-line Data Catalog: VI/71A, SIMBAD, CDS, Strasbourg
de Zeeuw, P. T., Hoogerwerf, R., & de Bruijne, J. H. J. 1999, AJ, 117, 354
ESA, 1997, The Hipparcos and Tycho Catalogues (ESA SP-1200; Noordwijk: ESA)
Flower, P. J. 1996, ApJ, 469, 355
Hearnshaw, J. B., Barnes, S. I., Kershaw, G. M., Frost, N., Graham, G., Ritchie, R., & Nankivell, G. R. 2002, ExA, 13, 59
Hensberge, H. et al. 2007, MNRAS, 379, 349
Hosokawa, Y. 1958, ReToh, 61, 4
Hubrig, S., Le Mignant, D., North, P., & Krautter, J. 2001, A&A, 372, 152
Idaczyk, R. 2012, VSS Newsl., 3, 8
Nitschelm, C. 2004, ASPC, 318, 291
Preibisch, T., & Mamajek, E. 2008, Handbook of Star Forming Regions, II: The Southern Sky, ed. B. Reipurth (ASP Monograph Publications, 5; San Francisco, CA: ASP), 235
Ralchenko, Yu., Kramida, A., & Olsen, K. 2011, NIST Atomic Spectra Database, Ver. 4 (Washington, DC: US Department of Commerce)
Renson, P., & Manfroid, J. 2009, A&A, 498, 961
Rhodes, M. D. 2008, CurveFit Manual, http://home.comcast.net/michael.rhodes/
Rucinski, S. M. 2002, AJ, 124, 1746
Sartori, M. J., Lépine, J. R. D., & Dias, W. S. 2003, A&A, 404, 913
Siess, L., Dufour, E., & Forestini, M. 2000, A&A, 358, 593
Skuljan, J., Ramm, D. J., & Hearnshaw, J. B. 2004, MNRAS, 352, 975
Skuljan, J., & Wright, D., 2007, HERCULES Reduction Software Package (HRSP), Ver. 3 (Christchurch, New Zealand: University of Canterbury)
Slawson, R. W., Hill, J., & Landstreet, J. D. 1992, ApJS, 82, 117
Sokolov, N. A. 1995, A&AS, 110, 553
Tokovinin, A. A. 1997, A&AS, 124, 75
Van Hamme, W. 1993, AJ, 106, 2096
Vaz, L. P. R., Andersen, J., & Claret, A. 2007, A&A, 469, 285
Vogt, N., & Faúndez, A. M. 1979, A&AS, 36, 477
Von Zeipel, H. 1924, MNRAS, 84, 702
Zahn, J.-P. 1977, A&A, 57, 383